Temperature-dependent spin dynamics in Cr$_2$O$_3$

Qiyang Sun,[1] Bin Wei [ORCID],[2] Yaokun Su [ORCID],[3] Douglas L. Abernathy [ORCID],[4] and Chen Li [ORCID][1,3]

[1]*Mechanical Engineering, University of California, Riverside, Riverside, California 92521, USA*

[2]*Henan Key Laboratory of Materials on Deep-Earth Engineering, School of Materials Science and Engineering,*
Henan Polytechnic University, Jiaozuo 454000, China

[3]*Materials Science and Engineering, University of California, Riverside, Riverside, California 92521, USA*

[4]*Neutron Scattering Division, Oak Ridge National Laboratory, Oak Ridge, Tennessee 37830, USA*

Cr$_2$O$_3$ emerges as a prominent candidate material for spintronics and magnetoelectronic applications. However, a comprehensive understanding of its temperature-dependent spin dynamics remains elusive, impeding the engineering of novel spintronics based on this material. We delve into this through a combination of inelastic neutron scattering experiments and atomistic simulations. Our results unveiled the emergence of paramagnons above and below T_N. We demonstrated a significant softening of linear magnons upon heating in the antiferromagnetic state. Further analysis revealed that this softening primarily originated from four-magnon interactions, while thermal expansion played a minor role.

I. INTRODUCTION

Mott-Hubbard antiferromagnetic (AFM) insulators are promising for ultrafast spintronics [1–4], memory devices [5], and spin-caloritronic applications [6,7]. AFMs offer advantages over ferromagnets for spintronics, including robustness against external fields, negligible stray fields, ultrafast spin dynamics, and potential room-temperature operation. While spin transport in AFMs is an emerging field with challenges around efficient spin current generation, detection, and control of the antiferromagnetic order, overcoming these hurdles could enable novel high-performance spintronic devices leveraging AFMs. Characterizing and predicting temperature-dependent spin dynamics is central to the engineering of spin transport.

Chromia (Cr$_2$O$_3$) is of particular interest because it is also the prototypical magnetoelectric material that is promising for magnetic field sensors, voltage-tunable inductors, and mechanical magnetoelectric antennas. Below the Néel temperature ($T_N = 307$ K), it has a corundum-type crystal structure with lattice parameters of $a = b = 4.95$ Å and $c = 13.57$ Å, and belongs to space group 167 ($R\bar{3}C$) [8]. It has a collinear AFM spin ordering with easy-axis anisotropy along the c axis, breaking both inversion and time reversal symmetries. In Cr$_2$O$_3$ thin films, the magnetoelectric coupling allows the manipulation of magnon polarization using an electric field [9]. A recent study highlights the formation of magnon-phonon polarons in Cr$_2$O$_3$ at low temperatures, demonstrating the potential to control spin transport via lattice excitation [10]. Previous neutron scattering experiments have provided detailed characterizations of the magnetic structure and spin dynamics [11], but temperature-dependent spin dynamics remain unexplored.

In this work, we use inelastic neutron scattering (INS) experiments to characterize temperature-dependent spin dynamics. Atomistic calculations were performed to model INS intensities from linear magnons and separate those from damped magnetic excitations (DMEs), i.e., so-called paramagnons, at high temperatures. Theoretical quantifications of magnon energy renormalization by thermal expansion and magnon-magnon scattering are presented.

II. EXPERIMENT

Time-of-flight INS measurements were performed on single-crystal and polycrystalline Cr$_2$O$_3$ samples to investigate their dynamic properties. A cylindrical (10 mm in diameter and 5 mm in length) single crystal of 99.99% purity with a mass of 2.6 grams was used. Both the single crystal and the polycrystalline (99.97% metal-based purity) samples were purchased commercially. The experiments were carried out using the wide angular range chopper spectrometer (ARCS) at the spallation neutron source (SNS). The samples were mounted on aluminum holders inside a low-background electrical resistance vacuum furnace. For the single-crystal Cr$_2$O$_3$ sample, four-dimensional dynamic structure factors were obtained at temperatures of 50, 280, and 450 K, using an incident energy of 75 meV. Data reduction was performed using MANTID [12], with normalization by the proton current on the target and correction for detector efficiency. Two-dimensional momentum-energy ($\mathbf{Q}$-E) views of dispersions were obtained by slicing the data along high symmetry directions in reciprocal space. For the polycrystalline Cr$_2$O$_3$ sample, two-dimensional dynamic structure factors were obtained at temperatures of 50, 150, 280, 350, and 450 K, using an incident energy of 100 meV. To account for the background from the sample holder, INS measurements were performed on an empty can at the same temperatures, and the measured intensity was subtracted from the polycrystalline data.

III. RESULT AND DISCUSSIONS

Two-dimensional $S(\mathbf{Q}, E)$ slices at low neutron momentum transfer ($\mathbf{Q}$) along the [0,0,L] direction are shown
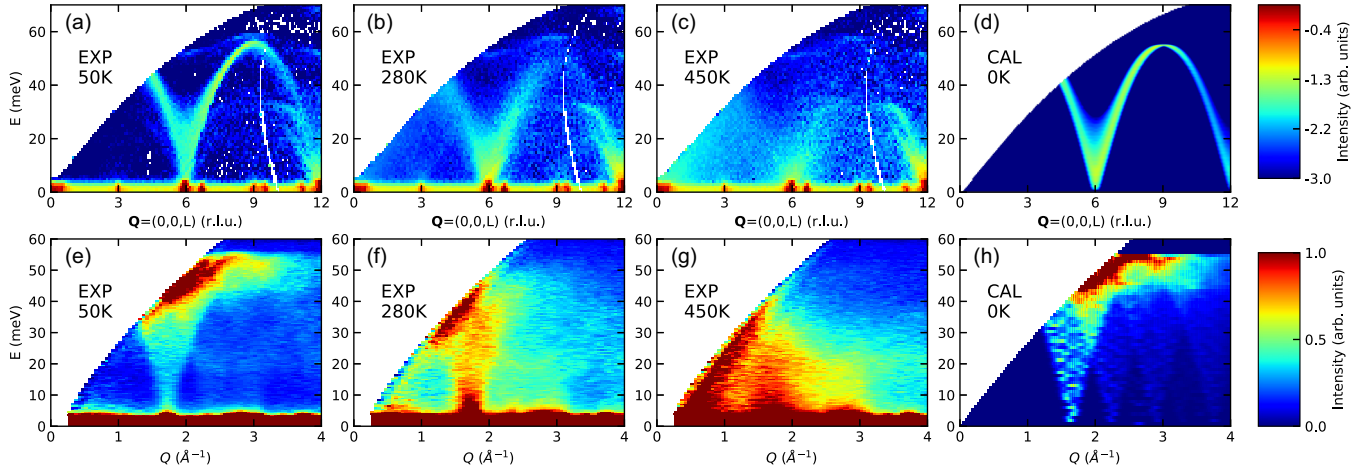
FIG. 1. The temperature-dependent measured and calculated dynamic structure factor of Cr_2O_3. (a), (b), (c) The dynamic structure factor of single crystal Cr_2O_3 measured by INS on ARCS at 50, 280, and 450 K along the [0,0,L] direction in the reciprocal space. The intensity is integrated over ± 0.2 (r.l.u) along the perpendicular axes. (d) Simulation of magnetic scattering $S(\boldsymbol{Q}, E)$ at 0 K with the same $\boldsymbol{Q}$ integration ranges. Both experimental data and theoretical calculations are plotted on a logarithmic scale. (e), (f), (g) The measured $S(E)$ function of polycrystalline samples at 50, 280, and 450 K at low $\boldsymbol{Q}$s. (h) The calculated $S(E)$ function at 0 K. In (d) and (h), both calculated S(E) and $S(\boldsymbol{Q}, E)$ are cropped by the neutron scattering kinetic limits and convoluted with the instrument resolution function.

in Figs. 1(a)–1(c). At 50 K, the magnon dispersion from L = 6 (r.l.u.) reaches its maximum energy ($\sim$55 meV) at L = 9. In Fig. 1(e), polycrystalline INS data also show an energy cutoff of 55 meV at 50 K. From our calculations (see note 1 in the Supplemental Material), we found $J_1 = -15$ meV, $J_2 = -6.8$ meV, and $J_3 = -0.5$ meV, which align very well with the measurements, as can be seen by comparing Figs. 1(a) to 1(d) and 1(h) to 1(e); Figs. S3(a) to S3(b) and S3(c) to S3(d). These exchange parameters significantly differ from the results of a previous piezospectroscopic study for exchange-coupled Cr^{3+} in ruby ($J_1 = -28$ meV, $J_2 = -12$ meV, and $J_3 = -1.4$ meV) [13] and (nearly two times of) previous neutron scattering work on Cr_2O_3 ($J_1 = -7.4$ meV, $J_2 = -3.3$ meV, and $J_3 = -0.2$ meV) [11]. The latter difference may arise from double counting of exchange neighbors in their analytical model, although the model also predicts the magnon dispersion well. On the other hand, the ratio, $J_2/J_1 = 0.45$, is in agreement with the neutron scattering work [11] while disagreeing with the theoretical predictions of $J_2/J_1 = 0.7$ [14]. In Fig. 1(c), the strong scattering intensities near L = 6 indicate the existence of paramagnons at 450 K. For better illustration, constant-E slices were obtained by integrating $10 < E < 30$ meV to investigate Q and temperature dependence. As shown in Fig. 2(a), the calculated lattice + magnetic scattering intensities (see notes 1 and 2 in the Supplemental Material [15]) show excellent agreement with the measured intensity at 50 K, proving the reliability of the method. At 450 K, the measured intensities near L = 6 cannot be solely modeled by lattice scattering [see Fig. 2(c)], and the sizable difference in intensities is from INS by paramagnons. Compared to 50 K data, paramagnons above T_N have much lower energies and shorter lifetimes. The damped paramagnon intensities disappear above 35 meV and significantly broaden, as shown in Fig. 1(c). The paramagnons have an energy range similar to that of longitudinal acoustic phonons (LA) near L = 6 and 12. The weak intensities from LA near

L = 6 are unlikely from magnetovibrational scattering, as was observed in nickel oxide [16], because they are absent at 50 K.

In the context of this study, it is crucial to distinguish a magnon and a paramagnon. They are both collective quantum excitations. Magnons emerge in the ordered phase and arise from the alignment of neighboring spins. In contrast, paramagnons manifest in the paramagnetic (PM) phase at high temperatures, where thermal energy dominates, leading to a nonmagnetic average state. Instead of long-range spin correlation, the paramagnons arise from coupling within or between short-range magnetic clusters in materials [17]. The intensity of magnetic Bragg reflection is subject to the spin-spin pair correlation function, which, on a statistical average, is proportional to the sublattice magnetization and reflects the long-range spin order. We analyzed the intensity variation of magnetic Bragg reflection at $|\boldsymbol{Q}| = 1.72$ Å^{-1} with temperature. As shown in Fig. S1 of the Supplemental Material, the magnetic Bragg peaks vanish above T_N, indicating long-range spin order is lost in the paramagnetic phase. The emergence of paramagnons is beyond the theory of linear magnon, which is based on small perturbations on the long-range spin correlations. Instead, they arise from short-range magnetic order and undergo diffuse transport, suggesting that the entropy of the spin degree of freedom is not yet maximized at 450 K.

At 280 K, scattering intensities near L = 6 cannot be solely modeled by magnetic INS by linear magnons, suggesting the presence of overdamped magnetic excitation. On the neutron energy loss side, the magnetic scattering cross section can be written as

$$\frac{d\sigma^2}{d\Omega dE} = A|F(\boldsymbol{Q})|^2 e^{-2W} \frac{\chi''(\boldsymbol{Q}, E)}{1 - e^{-E/k_B T}}, \quad (1)$$

where A contains temperature-independent INS coefficients, $F(\boldsymbol{Q})$ is the magnetic form factor of Cr^{3+}, e^{-2W} is the Debye-Waller term, and $\chi''(\boldsymbol{Q}, E)$ is the generalized susceptibility. $1/(1 - e^{-E/k_B T})$ is the thermal occupation factor, where k_B is
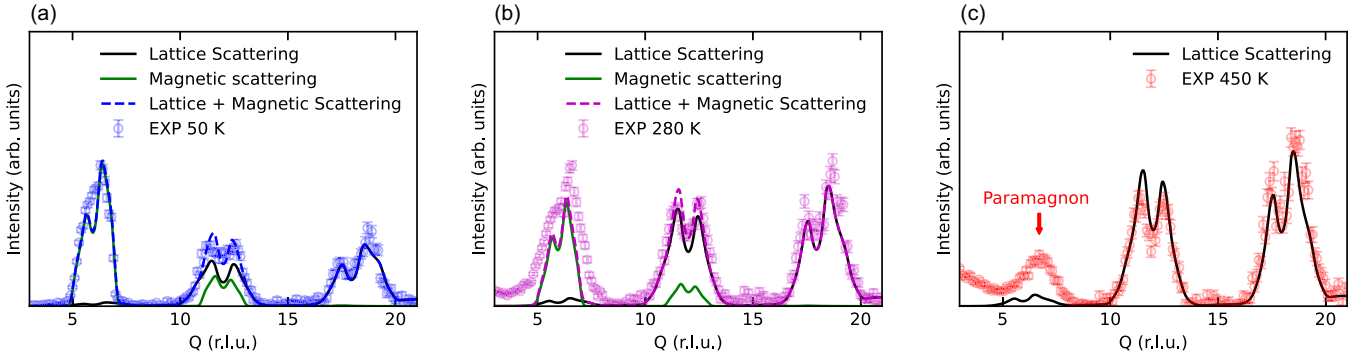
FIG. 2. Evidence of paramagnons and short-range correlation near and above T_N. (a), (b), (c) The measured constant-E slices at 50, 280, and 450 K compared with the atomistic simulations. Colored dots represent the intensities obtained by integrating $10 < E < 30$ meV of the measured data along [0,0,L] with background subtraction. The error bars indicate uncertainties in the data. The simulation of magnetic (lattice) scattering intensity at the same temperature with the same integration range is shown by the green line (black line), and the magnetic + lattice scattering intensity is indicated by blue (50 K) and purple (280 K) dashed lines.

the Boltzmann constant and T is the temperature. Assuming that the magnetic form factor and the Debye-Waller term change little with temperature, the temperature dependence of the magnetic INS intensity is subject to that of $\chi''(\mathbf{Q}, E)$. Neglecting magnon energy renormalization, the variation of $\chi''(\mathbf{Q}, E)$ depends on sublattice magnetization and can be modeled by the variation of magnetic Bragg peak intensity I on heating. The magnetic intensity at T can be represented using that at 0 K,

$$\frac{d\sigma^2}{d\Omega dE}(T) = \frac{1}{1 - e^{-E/k_B T}} \frac{I_{(T)}}{I_{(0K)}} \frac{d\sigma^2}{d\Omega dE}(0K). \quad (2)$$

As shown in Fig. 2(b), the measured intensity is nontrivial at $L < 6$ and is stronger than the calculated results for INS by magnons. The ratio between calculated and experiment magnetic INS intensity by integrating $4 < L < 8$ is 0.54, suggesting that nearly half of magnetic intensities at 280 K originate from paramagnons, similar to 450 K. The coexistence of magnons and paramagnons below T_N is seldom discussed, yet it is expected because only ∼33% of long-range spin order is preserved at this temperature [see Fig. S1(b) in the Supplemental Material], and such paramagnons can arise from short-range spin order. Note that excluding the Debye-Waler effect overestimates the calculated scattering intensity and would not change the result.

Paramagnons are also observed in the measured magnon density of states (DOS) by polycrystalline INS at 280 K. The data were obtained by integrating $2.5 < |\mathbf{Q}| < 4$ Å^{-1} to avoid the no-data region limited by neutron scattering kinetic limit and with background subtractions using data from $4 < |\mathbf{Q}| < 4.5$ Å^{-1} to remove lattice scattering. The quasielastic diffuse scattering intensity was removed (see Fig. S2 in the Supplemental Material), and thermal occupation corrections were applied. Above T_N, the measured 350 and 450 K data show clear bumps spanning a broad energy range centered near 25 meV, showing the feature of paramagnons [see Fig. 3(b)]. These differ from 50 and 150 K data, where the intensities are much weaker due to steep slopes of magnon dispersions and small magnon DOS in this energy range. The bumps are not likely from INS by magnons because linearlike magnon dispersions lead to an E^2 dependence in DOS, as shown by

the scattering intensities at 50 and 150 K below 35 meV in Fig. 3(b). The paramagnon scattering weakened from 350 to 450 K, suggesting a gradual weakening of short-range spin correlations as the temperature increases further above T_N. Notably, a similar bump that does not follow the E^2 trend also shows up at 280 K, supporting the presence of paramagnons.

In the AFM phase, the entire magnon dispersion along the [0,0,L] direction shows a 13% softening from 50 to 280 K, as shown in Figs. 1(a) and 1(b). The softening of magnon energies is also observed in the data from polycrystalline measurements shown in Fig. 3(b). To obtain pure magnon intensity at 280 K, the intensity of paramagnons was subtracted using 450 K data with a factor of 0.66, as shown in Figs. 3(b) and 3(e). The ratio of the linear magnon intensity to the total intensity is 0.54, consistent with the ratio obtained from single crystal results. In Fig. 3(d), the average magnon energies are represented by the center of mass of the measured data. The average magnon energy at 50 K is 45.7 meV, showing 5% and 14% softening from 50 to 150 K and 50 to 280 K, respectively.

To include the effects of temperature change on magnon energy, we consider the magnon system described by the Hamiltonian $\mathcal{H} = \mathcal{H}_{\text{non-int}} + \mathcal{H}_{\text{int}}$, where $\mathcal{H}_{\text{non-int}}$ contains the ground state energy E_0 and the total energy of noninteractive magnons $\sum_k \hbar \omega_k c_k^\dagger c_k$, and the $\mathcal{H}_{\text{int}}$ represents the interactions of magnons with themselves and other elementary excitations in the crystal, such as phonons. We first consider the effect of thermal expansion on $\mathcal{H}_{\text{non-int}}$. Thermal expansion modifies the overlaps of electron orbitals and consequently changes the exchange coupling and the anisotropy energy. The anisotropy term changes little with heating because the spin wave bandgap is ∼0.68 meV [11]. The lattice deformation is known to result in a nontrivial change in the exchange coupling constants [18], and the temperature dependence of $\mathcal{H}_{\text{non-int}}$ is subject to that of the exchange coupling constants J_n.

Ab initio density functional theory (DFT) calculations were performed using the Vienna *ab initio* simulation package (VASP) [19,20] with a plane-wave basis set and projector augmented wave (PAW) pseudopotentials [21,22]. Generalized gradient approximation (GGA) exchange-correlation functionals [23] and the Hubbard-U model [24] with
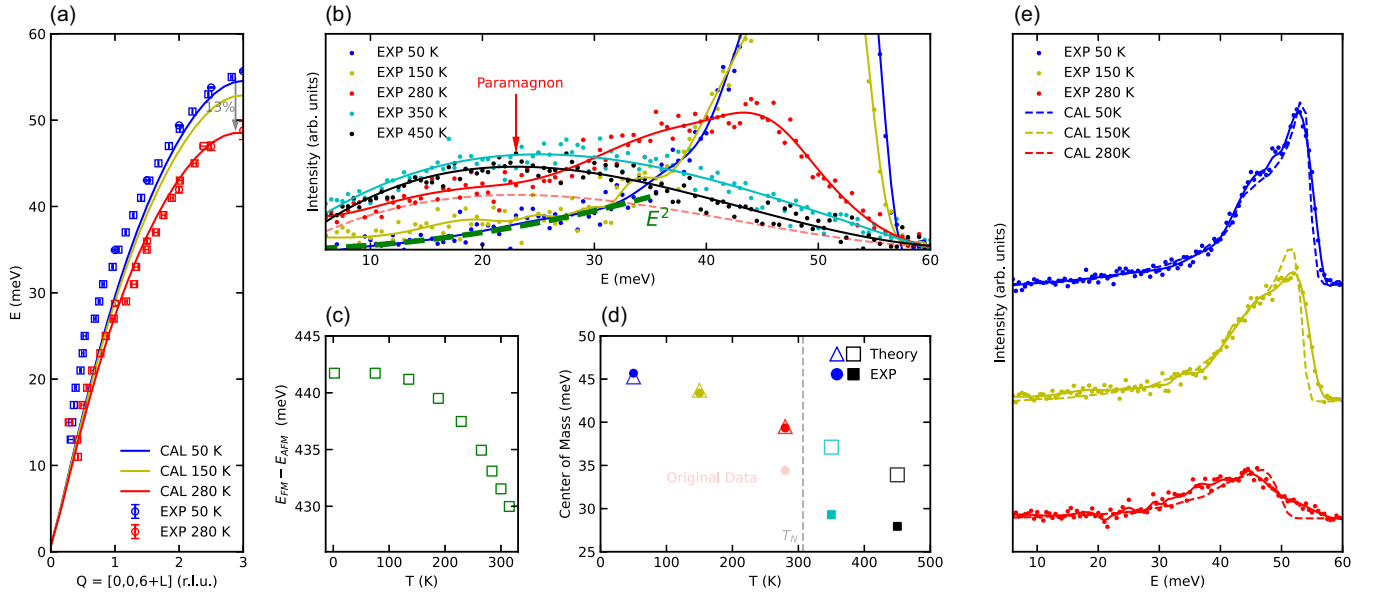
FIG. 3. Temperature-dependent magnon energy shifts from experiments and theories. (a) The measured and the calculated magnon dispersions at 50 and 280 K in the [0,0,L] direction. The experimental magnon energies were extracted from Gaussian fittings of the constant-Q (circles) and constant-E (squares) of the measured $S(Q, E)$ at 50 (blue) and 280 (red) K. The error bars represent fitting uncertainties. (b) Dots show measured scattering intensity from polycrystalline samples at 50, 150, 280, 350, and 450 K. Curves are guides for the eyes. The quasielastic diffuse scattering intensities were removed, and the data were corrected by thermal occupation. The red dashed line shows intensity from paramagnons at 280 K. (c) Green dots show the temperature-dependent total energy difference between the AFM and FM spin configurations (see text). (d) Solid (empty) markers show the center of mass of the measured (calculated) $S(Q, E)$, which is indicative of magnon softening. The 280 K data without paramagnon intensity subtraction is shown by the light red dot. (e) The measured polycrystalline data (dots, curves are eye guides.) are compared with magnon DOS calculations (see text) at 50, 150, and 280 K. The 280 K INS data were obtained by subtracting paramagnon intensities (see text). The calculated curves were convoluted with the instrument resolution function and normalized to the sublattice magnetization.

$U - J = 3.5$ eV were used. An energy cutoff of 550 eV was used for all calculations. The conventional unit cell containing 12 chromium and 18 oxygen atoms was used with a Γ-centered k-point grid of $9 \times 9 \times 9$. The temperature-dependent electronic total energies of collinear AFM and FM spin order are calculated with the literature lattice constants [25], for which the *ab* axes expand and the *c* axis contracts with the increase in temperature, and both are nonlinear.

In Fig. 3(c), the energy difference $\Delta E = E_{FM} - E_{AFM}$ corresponds to two times of $\mathcal{H}_{\text{non}-\text{int}}$ for 12 Cr and 18 O atoms and agrees with $-12J_1 - 36J_2$ obtained from our INS data (424.8 meV). The obtained ΔE decreases little with temperature-induced thermal expansion (2% from 2 to 284 K), indicating a slight weakening of the exchange interaction strengths on thermal expansion. The magnon energies depend linearly on exchange parameters. Clearly, the observed softening of magnon energies ($13 \sim 14\%$) cannot be solely explained by thermal expansion with the noninteractive magnon picture.

Magnon interactions are related to the scattering processes, which cause both the renormalization of the magnon energy and the reduction of the magnon lifetime. In Cr_2O_3, the magnon-electron scattering process is mostly absent due to the large electron band gap (3.37 eV) [26]. Three-magnon scattering, four-magnon scattering, and magnon-phonon scattering contribute to the $\mathcal{H}_{\text{int}}$. Notably, the three-magnon interactions arise from the dipolar energy and do not contribute to the magnon energy renormalization [27,28]. We

considered the four-magnon scattering due to the exchange interaction [28,29],

$$\mathcal{H}_{\text{exc}}^4 = \sum_i \frac{z_i J_i}{4N} \sum_{\substack{k_1, k_2 \\ k_3, k_4}} \Delta(k)[\gamma_i(k_1) + \gamma_i(k_2) + \gamma_i(k_3)$$
$$+ \gamma_i(k_4) - 4\gamma_i(k_4 - k_1)]c_{k_1}^\dagger c_{k_2}^\dagger c_{k_3} c_{k_4}, \quad (3)$$

where z_i is the number of ith nearest neighbors, N is the number of spins in the crystal, J_i is the exchange parameter for ith nearest neighbors, and γ_i (k) is the structure factor defined by

$$\gamma_i(k) = \frac{1}{z_i} \sum_{\vec{\delta}} e^{ik \cdot \delta_i}, \quad (4)$$

where δ_i represents the vector connecting a spin to its z_i nearest neighbors. We approximate $\mathcal{H}_{\text{exc}}^4$ by considering two modes, the magnon of interest with wave vector k and another magnon k'. The k and k' correspond to any of the four wave vectors in $\mathcal{H}_{\text{exc}}^4$. This approximation may underestimate the scattering phase space of the four-magnon process. Using the random-phase approximation, $c_{k'}^\dagger c_{k'} \rightarrow \langle c_{k'}^\dagger c_{k'} \rangle = \langle n_{k'} \rangle$, the magnon energy renormalization reads [28–30]

$$\hbar \Delta \omega_k = \sum_i \frac{2z_i J_i}{N_k} \sum_{k'} (1 + \gamma_i(k - k')$$
$$- \gamma_i(k) - \gamma_i(k'))\langle n_{k'} \rangle, \quad (5)$$

where N_k is the number of $\boldsymbol{k}$ points and $\langle n_{k'} \rangle$ is the Bose-Einstein distribution,

$$\langle n_{k'} \rangle = \frac{1}{e^{\hbar \omega_{k'}/k_B T} - 1}. \tag{6}$$

The magnon energy renormalization was quantitatively evaluated based on the analytical magnon dispersion in Ref. [11] as $\omega_k(0K)$. We chose $N_k = 64\,000$ with a $40 \times 40 \times 40$ mesh in the reciprocal space. We considered exchange interactions up to the second nearest neighbors with $J_1 = -15\,\mathrm{meV}$ and $J_2/J_1 = 0.5$. Each spin has one nearest neighbor and three second nearest neighbors ($z_1 = 1$ and $z_2 = 3$). In the first cycle, $\Delta \omega_k(T)$ was evaluated based on $\omega_k(0K)$, and the magnon energies were updated by $\omega_k(T) = \omega_k(0K) - \Delta \omega_k(T)$. In the following cycles, Bose-Einstein factors are evaluated based on the renormalized magnon energies and produce new $\Delta \omega_k(T)$. These were repeated until convergence when the change of $\Delta \omega_k(T)$ is less than 0.1% for all points. The magnon energies at $T = 50$, 150, and 280 K were obtained by subtracting the converged $\Delta \omega_k(T)$ from $\omega_k(0K)$.

Figures 3(a) and 3(e) show the experiment-theory comparison of magnon dispersion along [0,0,L] and DOS, respectively. In Fig. 3(e), the calculated magnon DOS were convoluted with instrumental resolution and normalized by sublattice magnetization (see Fig. S1 in the Supplemental Material) to compare directly with our polycrystalline data. The calculated temperature-dependent magnon dispersion and magnon DOS align well with our INS data. The calculation predicts 11.1% of energy softening from 50 to 280 K. This and the 2.0% softening induced by thermal expansion reach an excellent agreement with the softening observed from INS data ($\sim$13%). Our results suggest that magnon-magnon scattering dominates magnon energy renormalization, whereas the effect of thermal expansion on exchange coupling plays a minor role. These also imply that magnon-phonon scattering does not play a significant role.

In Fig. 3(d), the energies of the center of mass of the calculated magnon DOS are consistent with that obtained from INS data at 50 and 150 K, and data with paramagnon intensity subtraction at 280 K. The inconsistency between the calculation and the original INS data at 280 K supports the hypothesis that the bump intensity does not come from linear magnons. While the calculated DOS is in good agreement with 50 and 150 K INS data in line shapes, the measured spectrum at 280 K is wider than the calculated DOS. The broadening is also seen in the single crystal data at 280 K, as shown in Fig. 1(b). Due to steep magnon dispersion, it is challenging to directly compare magnon energy linewidth from finite integration in the reciprocal space at temperatures. Instead, we obtain the $\boldsymbol{Q}$ linewidth of magnon dispersion measured by INS. The larger the $\boldsymbol{Q}$ linewidths, the larger the magnon E linewidths. Constant-E slices were obtained both from INS data and simulated magnon intensities shown in Figs. 1(a), 1(b), and 1(d). The $\boldsymbol{Q}$ positions and $\boldsymbol{Q}$ linewidths were extracted from Gaussian fittings. In Fig. 4, a great agreement between structure factor calculation and experiment data at 50 K is shown, indicating that at 50 K, the $\boldsymbol{Q}$ linewidth majorly comes from instrument resolution. However, our data at 280 K show a significant broadening of $\boldsymbol{Q}$ linewidth, indicating the shortening of
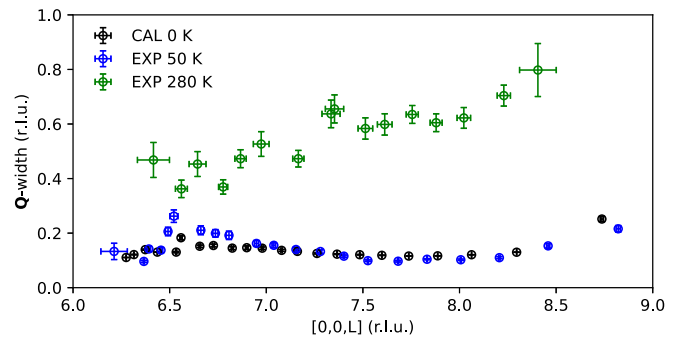

FIG. 4. $\boldsymbol{Q}$-dependent experimental and theoretical $\boldsymbol{Q}$-linewidths obtained from constant-E slices along the [0,0,L] direction. Horizontal and vertical error bars represent fitting errors.

magnon lifetimes. This suggests strong magnon interactions and supports the idea that magnon scattering causes magnon energy renormalizations. Such broadening may originate from the intrinsic shortening of magnon lifetimes, which indicates the magnon scattering as the primary source of energy softening.

In addition, we performed calculations at 350 and 450 K to predict the energy softening of linear magnons above T_N. The center of mass from calculated DOS shows a linear decrease from 280 to 450 K. The results disagree with INS data at 350 and 450 K, indicating that these low-energy paramagnons are not a result of the magnon softening. Theoretical quantifications of paramagnon energies through Monte Carlo simulations and cluster mean-field theory [17] are beyond the scope of the current study.

IV. CONCLUSION

To conclude, our findings reveal that the magnetic excitations observed below the T_N are comprised of two distinct components: one emanating from damped magnons arising from magnon interactions and the other originating from paramagnons that emerge due to the coupling within or between short-range spin clusters. Our results indicate that the four-magnon process is the primary contributor to the softening of linear magnons, and thermal expansion plays a secondary role. These results illuminate the intricate behaviors of these magnetic excitations near T_N, providing valuable insights into characterizing and controlling the spin dynamics of Cr_2O_3 for functional spintronics and magnetoelectronic applications.

ACKNOWLEDGMENTS

[1] O. Gomonay, T. Jungwirth, and J. Sinova, High antiferromagnetic domain wall velocity induced by Néel spin-orbit torques, Phys. Rev. Lett. **117**, 017202 (2016).

[2] C. Tzschaschel, K. Otani, R. Iida, T. Shimura, H. Ueda, S. Günther, M. Fiebig, and T. Satoh, Ultrafast optical excitation of coherent magnons in antiferromagnetic NiO, Phys. Rev. B **95**, 174407 (2017).

[3] M. Fechner, A. Sukhov, L. Chotorlishvili, C. Kenel, J. Berakdar, and N. A. Spaldin, Magnetophononics: Ultrafast spin control through the lattice, Phys. Rev. Mater. **2**, 064401 (2018).

[4] Y. W. Windsor, D. Zahn, R. Kamrla, J. Feldl, H. Seiler, C. T. Chiang, M. Ramsteiner, W. Widdra, R. Ernstorfer, and L. Rettig, Exchange-striction driven ultrafast nonthermal lattice dynamics in NiO, Phys. Rev. Lett. **126**, 147202 (2021).

[5] T. Jungwirth, X. Marti, P. Wadley, and J. Wunderlich, Antiferromagnetic spintronics, Nat. Nanotechnol. **11**, 231 (2016).

[6] G. E. Bauer, E. Saitoh, and B. J. van Wees, Spin caloritronics, Nat. Mater. **11**, 391 (2012).

[7] S. R. Boona, R. C. Myers, and J. P. Heremans, Spin caloritronics, Energy Environ. Sci. **7**, 885 (2014).

[8] L. W. Finger and R. M. Hazen, Crystal structure and isothermal compression of Fe_2O_3, Cr_2O_3, and V_2O_3 to 50 kbars, J. Appl. Phys. **51**, 5362 (1980).

[9] C. Liu, Y. Luo, D. Hong, S. S.-L. Zhang, H. Saglam, Y. Li, Y. Lin, B. Fisher, J. E. Pearson, J. S. Jiang, H. Zhou, J. Wen, A. Hoffmann, and A. Bhattacharya, Electric field control of magnon spin currents in an antiferromagnetic insulator, Sci. Adv. **7**, eabg1669 (2021).

[10] J. Li, H. T. Simensen, D. Reitz, Q. Sun, W. Yuan, C. Li, Y. Tserkovnyak, A. Brataas, and J. Shi, Observation of magnon polarons in a uniaxial antiferromagnetic insulator, Phys. Rev. Lett. **125**, 217201 (2020).

[11] E. J. Samuelsen, M. T. Hutchings, and G. Shirane, Inelastic neutron scattering investigation of spin waves and magnetic interactions in Cr_2O_3, Physica **48**, 13 (1970).

[12] O. Arnold, J. C. Bilheux, J. M. Borreguero, A. Buts, S. I. Campbell, L. Chapon, M. Doucet, N. Draper, R. Ferraz Leal, M. A. Gigg, V. E. Lynch, A. Markvardsen, D. J. Mikkelson, R. L. Mikkelson, R. Miller, K. Palmen, P. Parker, G. Passos, T. G. Perring, P. F. Peterson *et al.*, Mantiddata analysis and visualization package for neutron scattering and μ sr experiments, Nucl. Instrum. Methods Phys. Res. Sect. A **764**, 156 (2014).

[13] L. Mollenauer and A. Schawlow, Piezospectroscopic studies of exchange-coupled Cr^{3+} ion pairs in ruby, Phys. Rev. **168**, 309 (1968).

[14] S. Shi, A. L. Wysocki, and K. D. Belashchenko, Magnetism of chromia from first-principles calculations, Phys. Rev. B **79**, 104404 (2009).

[15] See Supplemental Material at http://link.aps.org/supplemental/10.1103/PhysRevB.110.064413 for the details of the magnon and phonon scattering intensity calculations; elastic scattering intensities and analysis; experiment-theory comparisons of intensities along other high-symmetry directions; and data

analysis of the measured intensity from the polycrystalline samples, which also includes Refs. [8,11,31–33].

[16] Q. Sun, B. Wei, Y. Su, H. Smith, J. Y. Y. Lin, D. L. Abernathy, and C. Li, Mutual spin-phonon driving effects and phonon eigenvector renormalization in nickel (II) oxide, Proc. Natl. Acad. Sci. USA **119**, e2120553119 (2022).

[17] F. Heydarinasab, M. Jazandari, M. M. H. Polash, J. Abouie, and D. Vashaee, Paramagnon heat capacity and anomalous thermopower in anisotropic magnetic systems: Understanding interlayer spin correlations in a magnetically disordered phase, Phys. Rev. B **109**, 054418 (2024).

[18] Y. Kota, H. Imamura, and M. Sasaki, Effect of lattice deformation on exchange coupling constants in Cr_2O_3, J. Appl. Phys. **115**, 17D719 (2014).

[19] G. Kresse and J. Furthmüller, Efficient iterative schemes for *ab initio* total-energy calculations using a plane-wave basis set, Phys. Rev. B **54**, 11169 (1996).

[20] G. Kresse and J. Furthmüller, Efficiency of *ab-initio* total energy calculations for metals and semiconductors using a plane-wave basis set, Comput. Mater. Sci. **6**, 15 (1996).

[21] P. E. Blochl, Projector augmented-wave method, Phys. Rev. B **50**, 17953 (1994).

[22] G. Kresse and D. Joubert, From ultrasoft pseudopotentials to the projector augmented-wave method, Phys. Rev. B **59**, 1758 (1999).

[23] J. P. Perdew, K. Burke, and M. Ernzerhof, Generalized gradient approximation made simple, Phys. Rev. Lett. **77**, 3865 (1996).

[24] V. V. Anisimov, J. Zaanen, and O. K. Andersen, Band theory and Mott insulators: Hubbard U instead of Stoner I, Phys. Rev. B **44**, 943 (1991).

[25] A. H. Hill, A. Harrison, C. Dickinson, W. Zhou, and W. Kockelmann, Crystallographic and magnetic studies of mesoporous eskolaite, Microporous Mesoporous Mater. **130**, 280 (2010).

[26] R. Zimmermann, P. Steiner, and S. Hüfner, Electron spectroscopies and partial excitation spectra in Cr_2O_3, in *Proceedings of the 11th International Conference on Vacuum Ultraviolet Radiation Physics*, edited by T. Miyahara, Y. Azuma, M. Watanabe, and T. Ishii (Elsevier, Amsterdam, 1996), pp. 49–52.

[27] R. M. White, R. M. White, and B. Bayne, *Quantum Theory of Magnetism* (Springer-Verlag, Berlin, 1983), Vol. 1.

[28] S. M. Rezende, *Fundamentals of Magnonics* (Springer, Cham, 2020), Vol. 969, p. 301.

[29] D. S. Maior, E. C. Souza, and S. M. Rezende, Magnon energy renormalization in yttrium iron garnet, Phys. Rev. B **108**, 054406 (2023).

[30] S. M. Rezende, A. Azevedo, and R. L. Rodríguez-Suárez, Introduction to antiferromagnetic magnons, J. Appl. Phys. **126**, 151101 (2019).

[31] A. T. Boothroyd, *Principles of Neutron Scattering from Condensed Matter* (Oxford University Press, Oxford, UK, 2020).

[32] A. Togo and I. Tanaka, First principles phonon calculations in materials science, Scr. Mater. **108**, 1 (2015).

[33] H. Shaked and S. Shtrikman, Susceptibility derived sublattice magnetization in Cr_2O_3, Solid State Commun. **6**, 425 (1968).